Incorporation of Tb and Gd improves the diagnostic functionality of magnetotactic bacteria

Lucía Gandarias, Elizabeth Jefremovas, David Gandia, Lourdes Marcano, Virginia Martínez-Martínez, Pedro Ramos-Cabrer, Daniel M. Chevrier, Sergio Valencia, Luis Fernández Barquín, M. Luisa Fdez-Gubieda, et al.

Materials Today Bio 20 (2023) 100680

Contents lists available at ScienceDirect

Materials Today Bio

journal homepage: www.journals.elsevier.com/materials-today-bio

Incorporation of Tb and Gd improves the diagnostic functionality of magnetotactic bacteria

Lucía Gandarias [a,1,*], Elizabeth M. Jefremovas [b,c], David Gandia [d], Lourdes Marcano [e,f,g], Virginia Martínez-Martínez [h], Pedro Ramos-Cabrer [i,j], Daniel M. Chevrier [k], Sergio Valencia [f], Luis Fernández Barquín [b], M. Luisa Fdez-Gubieda [d,e], Javier Alonso [b], Ana García-Prieto [l,**], Alicia Muela [a]

[a] Dpto. Inmunología, Microbiología y Parasitología, Universidad del País Vasco (UPV/EHU), Leioa, 48940, Spain
[b] CITIMAC, Universidad de Cantabria, Santander, 39005, Spain
[c] Institut für Physik, Johannes Gutenberg Universität, Mainz, 55128, Germany
[d] BCMaterials, Bld. Martina Casiano 3rd Floor, Leioa, 48940, Spain
[e] Dpto. Electricidad y Electrónica, Universidad del País Vasco (UPV/EHU), Leioa, 48940, Spain
[f] Helmholtz-Zentrum Berlin für Materialien und Energie, Albert-Einstein-str. 15, Berlin, 12489, Germany
[g] Department of Physics, Faculty of Science, University of Oviedo, Oviedo, 33007, Spain
[h] Dpto. Química Física, Universidad del País Vasco (UPV/EHU), Leioa, 48940, Spain
[i] Center for Cooperative Research in Biomaterials (CIC BiomaGUNE), Basque Research and Technology Alliance (BRTA), Donostia-San Sebastián, 20014, Spain
[j] IKERBASQUE, Basque Foundation for Science, Bilbao, 48009, Spain
[k] Aix-Marseille Université, Centre national de la recherche scientifique (CNRS), Commissariat à l'énergie atomique et aux énergies alternatives (CEA), UMR7265, Bioscience and biotechnology institute of Aix-Marseille (BIAM), Saint-Paul-lez-Durance, 13108, France
[l] Dpto. Física Aplicada, Universidad del País Vasco (UPV/EHU), Bilbao, 48013, Spain

ARTICLE INFO

Keywords:
Magnetotactic bacteria
Theranostic agents
Luminescent markers
Magnetic resonance imaging
X-ray absorption spectroscopy
Magnetic hyperthermia

ABSTRACT

Magnetotactic bacteria are envisaged as potential theranostic agents. Their internal magnetic compass, chemical environment specificity and natural motility enable these microorganisms to behave as nanorobots, as they can be tracked and guided towards specific regions in the body and activated to generate a therapeutic response. Here we provide additional diagnostic functionalities to magnetotactic bacteria *Magnetospirillum gryphiswaldense* MSR-1 while retaining their intrinsic capabilities. These additional functionalities are achieved by incorporating Tb or Gd in the bacteria by culturing them in Tb/Gd supplemented media. The incorporation of Tb provides luminescence properties, enabling potential applications of bacteria as biomarkers. The incorporation of Gd turns bacteria into dual contrast agents for magnetic resonance imaging, since Gd adds T_1 contrast to the existing T_2 contrast of unmodified bacteria. Given their potential clinical applications, the diagnostic ability of the modified MSR-1 has been successfully tested *in vitro* in two cell models, confirming their suitability as fluorescent markers (Tb-MSR-1) and dual contrast agents for MRI (Gd-MSR-1).

1. Introduction

Magnetotactic bacteria (MTB) are aquatic microorganisms that synthesize internally chains of membrane-enclosed magnetic nanoparticles, called magnetosomes [1–4]. These magnetosome chains behave as a compass needle, allowing bacteria to orientate and navigate along the geomagnetic field lines.

MTB are envisaged as promising biomedical nanorobots (*nanobiots*) because they combine the guidance, control, and theranostic capabilities of magnetic nanoparticles with the motility, chemical specificity, and the capacity of being genetically modified of bacteria [5–7]. Moreover, MTB are non-pathogenic but can be modified to deliver and/or express certain

* Corresponding author.
** Corresponding author.
E-mail addresses: lucia.gandarias@ehu.eus (L. Gandarias), ana.garciap@ehu.eus (A. García-Prieto).
[1] Current address: Bioscience and Biotechnology Institute of Aix-Marseille (BIAM), UMR7265, Aix-Marseille Université, CNRS, CEA Cadarache, 13108 Saint-Paul-lez-Durance, France.

https://doi.org/10.1016/j.mtbio.2023.100680
Received 18 January 2023; Received in revised form 11 May 2023; Accepted 19 May 2023
Available online 24 May 2023

cytotoxic molecules. Several works have demonstrated the potential of magnetotactic bacteria as heating agents for magnetic hyperthermia [8–12], as drug delivery carriers [13–15], and as contrast agents for magnetic resonance imaging (MRI) [16–18] or magnetic particle imaging (MPI) [19].

Beyond the outstanding characteristics of MTB, a number of strategies have been developed to provide MTB with additional functionalities and improve their performance as biomedical agents for application. One approach comes from tuning their magnetic response, which relies on the magnetosome chains. In this line, even though the synthesis of magnetosomes is a process that is conducted under a strict genetic control, it has been shown that metallic elements can be incorporated into the magnetite mineral core of the magnetosomes, which results in significant changes of the bacterial magnetic properties. The incorporation of these elements can be achieved through a simple route that consists of growing the MTB in a culture medium supplemented with the metallic element [20–26].

Following this line, in a previous work we investigated the magnetic properties of the magnetotactic bacterium *Magnetospirillum gryphiswaldense* MSR-1 cultured in Tb or Gd supplemented media [27]. We showed that Tb^{3+} and Gd^{3+} were incorporated as dopants into the magnetite (Fe_3O_4) crystal structure of the magnetosome cores, substituting Fe^{3+} ions. Despite the minor incorporation, it was shown that the magnetic properties of the magnetosomes changed drastically at low temperatures, but remained unchanged at the temperature window of interest for biomedical applications. This means that no changes are expected in those functionalities of the modified bacteria which rely on the magnetic properties of the magnetosomes (*i.e.* guiding, tracking, or heating).

In this work, we focus on the potential biomedical applications of MSR-1 grown in the presence of Tb and Gd. We show that Tb and Gd are not only incorporated into the magnetite crystal cores of the magnetosomes, but are also found in other bacterial compartments. As a result of the presence of Tb and Gd in these other compartments, the modified bacteria achieve new functionalities that expand their potential as biomedical agents while retaining other intrinsic capabilities, such as the heating efficiency. Bacteria that incorporate Tb (and their isolated magnetosomes) are photoluminescent under UV irradiation, which provides them with enhanced diagnostic capabilities for *in vitro* studies. Alternatively, bacteria that incorporate Gd provide T_1 contrast for magnetic resonance imaging (MRI) in addition to the T_2 contrast of unmodified bacteria, thus serving as dual contrast agents, which recently have gained increased attention for their use in clinical MRI [28,29]. Finally, given their potential biomedical applications, the diagnostic ability of the modified MSR-1 has been successfully tested *in vitro* in two cell models, confirming their suitability as fluorescent markers (Tb-MSR-1) and dual contrast agents for MRI (Gd-MSR-1).

2. Materials and Methods

2.1. Bacterial growth conditions and magnetosome purification

Magnetospirillum gryphiswaldense strain MSR-1 (DMSZ 6631) was cultured at 28 °C for 48 h in Flask Standard Medium (FSM) [30] containing (per litre of deionized water) 0.1 g KH_2PO_4, 0.15 g $MgSO_4{\cdot}7H_2O$, 2.38 g HEPES, 0.34 g $NaNO_3$, 0.1 g yeast extract, 3 g soybean peptone, 0.3% (wt/vol) of sodium pyruvate as carbon source and 100 μM of Fe(III)-citrate. Tb-MSR-1 and Gd-MSR-1 were grown by supplementing the FSM media with 100 μM of Tb(III)-quinate and 100 μM of Gd(III)-quinate, respectively. This concentration was chosen after performing sensitivity curves of MSR-1 to increasing concentrations of Tb(III)-quinate and Gd(III)-quinate (see Fig. S1 in the Supplementary Information). Magnetosomes were isolated following the protocol described by Grünberg et al. [31] with minor modifications. Cells were collected by centrifugation, suspended in 20 mM HEPES/4 mM EDTA buffer (pH 7.4) and disrupted using a French Press (1250 psig). The lysed cells were then sonicated to disperse cell debris from magnetosomes and these were collected and washed 5 times using magnetic separation and 10 mM HEPES/200 mM NaCl buffer (pH 7.4). Finally, the isolated magnetosomes were suspended in ultrapure water.

2.2. Transmission electron microscopy (TEM)

Transmission electron microscopy (TEM) images were obtained of bacteria adsorbed onto 300 mesh carbon-coated copper grids, using a JEOL JEM-1400 Plus electron microscope at an accelerating voltage of 120 kV.

2.3. X-ray absorption near-edge structure (XANES)

Bacteria and isolated magnetosomes were measured at the Fe K-edge (7112 eV), and at Tb L_3 (7514 eV) and Gd L_3 (7243 eV) edges. Bacteria were collected by centrifugation after 48 h of culture. The obtained pellets were freeze-dried and compacted into 5 mm pills containing ~2 $\times 10^9$ bacteria. Isolated magnetosomes were freeze-dried and 2 mg of the obtained powder were mixed with 20 mg of boron nitride. The mixture was compacted into 5 mm pills.

X-ray absorption near-edge structure (XANES) spectra of the samples were collected at room temperature at the BL22-CLÆSS beamline of the ALBA synchrotron facility (Spain) using a double Si crystal oriented in the (111) direction as the monochromator. Measurements were performed in transmission configuration except for the Gd L_3-edge spectra of isolated magnetosomes, which were collected in fluorescence yield mode. Gd references ($GdCl_3$ (Sigma-Aldrich, 203289) and Gd_2O_3 (Alpha-Aesar, 11289)) were measured in transmission configuration, and the Tb reference ($Tb(NO_3)_3$) spectrum was kindly provided by Dr. Aida Serrano.

The experimental spectra were normalized using standard procedures for background subtraction and data normalization as implemented in the free software Athena of the IFEFFIT package [32,33].

2.4. Hard X-ray nanoprobe measurements

Scanning X-ray fluorescence microscopy (SXFM) measurements were carried out at the I-14 hard X-ray nanoprobe beamline (Diamond Light Source Ltd., Didcot, UK) [34]. Bacteria were deposited onto 300 mesh carbon-coated copper grids and mounted for measurement using custom holders designed and supplied by the beamline. Measurements were performed under ambient conditions using an incident photon energy of 8 (Gd) or 9 keV (Tb) with a focused X-ray beam of 50–60 nm (FWHM) in diameter. X-ray fluorescence (XRF) was collected in front of the sample using a four-element silicon drift detector (RaySpec, UK) with sample stage raster scanning step of 50 nm and a dwell time of 15 ms. A photon-counting Merlin detector (Quantum Detectors, UK) was used in transmission configuration to generate normalized phase-gradient (PG) images [35]. The data analysis was performed using PyMca [36] software to fit the fluorescence spectra taking into account the emission peaks of Fe ($K\alpha_1$ 6.405 keV), Tb ($L\alpha_1$ 6.273 keV), and Gd ($L\alpha_1$ 6.053 keV) to form the XRF images.

2.5. Magnetic hyperthermia

Magnetic hyperthermia studies were performed by AC magnetometry in a custom-made setup [37] using a frequency $f = 133$ kHz and a magnetic field amplitude ($\mu_0 H$) from 0 to 90 mT. The dynamic magnetization was measured for bacteria dispersed in Milli-Q water and at a concentration of 10^{11} bacteria mL^{-1}. The SAR values were obtained from the area (A) of the AC hysteresis loops according to Equation (1) [38]:

$$SAR\left(\frac{W}{g}\right) = \frac{f}{c}A = \frac{f}{c}\oint \mu_0 M_t \mathrm{d}H_t \quad (1)$$

where M_t is the instantaneous magnetization at time t, H_t is the sinusoidal

magnetic field of frequency f at time t, and c is the magnetite mass concentration in the dispersing medium. The integration is done over a period of the oscillating magnetic field, $T = 2\pi/f$. Given the low doping content of the magnetosomes, the magnetite mass concentrations (c) were calculated experimentally using the saturation magnetic moment of the DC hysteresis loops measured in a vibrating sample magnetometer and considering as a reference the saturation magnetization value of magnetite (92 $Am^2\ kg^{-1}$), resulting in $c = 0.24$ mg mL^{-1} for MSR-1, $c = 0.17$ mg mL^{-1} for Tb-MSR-1 and $c = 0.22$ mg mL^{-1} for Gd-MSR-1.

2.6. Luminescence measurements

Luminescence measurements of Tb-MSR-1 and Tb-magnetosomes were performed in a spectrofluorimeter Edinburgh Instruments (FLSP 920 model) with a Xenon flash lamp 450 W as the excitation source. The samples, in 1 cm optical path cuvettes in right-angle configuration, were excited with a $\lambda_{ex} = 285$ nm and the spectra were recorded at a $\lambda_{em} =$ 520–570 nm. For the culture medium not to interfere, it was removed by centrifugation and the bacteria were resuspended in Milli-Q water. The concentration of Tb-MSR-1 measured was 10^9 bacteria mL^{-1} and the concentration of Tb-magnetosomes was 50 μg mL^{-1}.

2.7. Fluorescence microscopy

Fluorescence microscopy images of Tb-MSR-1 and Tb-MSR-1-loaded eukaryotic cells were recorded with an optical inverted microscope with epi configuration (Olympus BX51) equipped with a X-CITE series 120Q fluorescent light source and a DP72 color CCD camera. Samples were excited with UV light by respective Chroma band-pass (350/50) and dichroic (380DCLP) filters and emission was collected with a Chroma cut-off filter from 500 nm (E515LPv2).

2.8. Magnetic resonance imaging (MRI)

MRI studies of MSR-1, magnetosomes, and eukaryotic cells, were conducted at 11.7 T using a Bruker Biospec 117/16 USR MRI system (Bruker Biospin GmbH, Ettlingen, Germany), interfaced to an advance III console and a BGA12S gradient insert of 660 mT m^{-1}. Images were acquired using a 4 cm inner diameter volumetric coil for radiofrequency transmission and reception (RX/TX) from Bruker and ParaVision 6.1 software from Bruker.

For bacteria and magnetosomes, T_2 relaxation was measured using a multi-slice multi-echo pulse (MSME) sequence acquiring a field of view of 32 × 32 mm (320 × 320 image matrix, giving an in-plane resolution of 100 × 100 μm) and acquiring 3 slices of 1 mm thickness with a 1 mm interslice gap. The main imaging parameters were: echo time TE = 32 consecutive echoes with values ranging between 5 and 135 ms (delta TE = 5 ms); repetition time TR = 4500 ms; Nav = 3 averages; SW = 163 kHz. The T_1 relaxation was measured using a variable TR rapid acquisition with relaxation enhancement (VTR-RARE) pulse sequence acquiring with the same field of view and matrix as for T_2. The main imaging parameters were: echo time TE = 6.87 ms (Rare factor = 2); 12 repetition times TR = 150, 386.5, 647.7, 939.4, 1269.8, 1650.5, 2099.8, 2647.9, 3350.9, 4332.6, 5972.0, 12500 ms; Nav = 3 averages; SW = 85 kHz.

In the case of eukaryotic cells, the T_2 maps were constructed by pixel-by-pixel fitting of MSME images of the agar/cells-filled Eppendorf tubes, acquired with the following parameters: field of view of 64 × 48 mm (213 × 160 image matrix, giving an in-plane resolution of 300 × 300 μm) acquiring 12 consecutive coronal slices of 1 mm thickness. Main imaging parameters were: echo time TE = 48 consecutive echoes with values ranging between 5.5 and 264 ms (delta TE = 5.5 ms); repetition time TR = 7.5 s; Nav = 1 averages; SW = 65 kHz. The T_1 maps were constructed by pixel-by-pixel fitting of RARE images of the agar/cells-filled Eppendorf tubes, acquired with same field of view and matrix as for T_2. The main imaging parameters were: echo time TE = 6.75 ms; 9 repetition times TR = 300, 700, 1200, 1800, 2400, 3000, 4500, 12500 ms; Nav = 1 averages; SW = 65 kHz.

T_1 and T_2 parametric maps were calculated pixel-by-pixel using self-developed routines for the NIH software Image-J, adjusting data to mono-exponential curves.

2.9. In vitro assays

A549 human lung carcinoma cells (DSMZ, ACC 107) and RAW 264.7 murine macrophages (ATCC, TIB-71) were cultured in RPMI medium supplemented with 10% fetal bovine serum, 2 mM L-glutamine and a mixture of antibiotics (100 U mL^{-1} penicillin and 100 μg mL^{-1} streptomycin) and 0.25 μg mL^{-1} amphotericin B (antimycotic) at 37 °C in a humidified atmosphere (95% relative humidity) and 5% CO_2. For cellular uptake of bacteria, 5×10^9 bacteria mL^{-1} were added to cell cultures containing 2×10^5 cell mL^{-1} in RPMI medium.

For the cytotoxicity assessment, the viability of cells cultured with bacteria was tested after 24 h and 48 h using flow cytometry (Beckman Coulter Gallios). In order to distinguish between living and dead cells, cells were stained with propidium iodide, a red fluorescent stain that links to DNA but can only penetrate the cells when their membranes are damaged, therefore staining only dead cells. It was excited with a blue laser (488 nm) and recorded in the FL3 channel (620/20 nm). To estimate cell concentration, commercial fluorescent beads from a known concentration were used (BD Trucount™ Tubes, 340334).

In order to measure the T_1 and T_2 contrast of eukaryotic cells (with or without bacteria), the samples were prepared by mixing 1:1 of ≈ 10^6 cells mL^{-1} and 1% agar in Eppendorf tubes where the measurements were carried out.

3. Results and discussion

3.1. Bacterial incorporation of Tb and Gd

The incorporation of Tb/Gd in MSR-1 was investigated by means of X-ray absorption near-edge structure (XANES) spectroscopy measured at the BL22-CLÆSS beamline at the ALBA synchrotron (Spain). This is an element-specific technique that allows determination of the oxidation state and coordination chemistry around the element of interest, here Fe and Tb or Gd, by selecting the energy of the incident X-ray energy around the Fe K- or Tb/Gd L_3-absorption edges.

XANES spectroscopy was previously used to analyze magnetosomes isolated from bacteria grown in presence of Tb or Gd [27]. These measurements indicated that Tb/Gd atoms are introduced in the crystal structure of the magnetite core of magnetosomes substituting approximately 3–4% of Fe^{3+} ions by Tb^{3+} or Gd^{3+}. Now, by measuring whole bacteria, we aim to discern whether Tb/Gd are also stored in other bacterial compartments apart from the magnetosomes.

Fe K-edge XANES measurements of bacteria grown in the presence of Tb or Gd (from now on designated Tb-MSR-1 and Gd-MSR-1, respectively) confirm that, as in MSR-1, the Fe is forming magnetite from the magnetosome cores, and is also found in a ferrihydrite-like phase as the one of bacterioferritin cores (see the Supplementary Information, Fig. S2). Alternatively, Fig. 1 shows the Tb/Gd L_3-edges XANES spectra of Tb-MSR-1 and Gd-MSR-1 and their corresponding isolated magnetosomes (Tb-mag and Gd-mag) together with Tb^{3+} and Gd^{3+} references ($Tb(NO_3)_3$ and $GdCl_3$, respectively). The position of the edge energy of the bacteria and isolated magnetosomes is coincident with the references, which indicates that the incorporated Tb/Gd ions are in the +3 oxidation state. We note the XANES spectra of whole bacteria and their corresponding isolated magnetosomes show distinct differences in the white line intensity (feature around 7520 and 7250 eV for Tb and Gd, respectively; attributed to the excitation of 2p core-level electrons to valence-level 5d orbital vacancies). The intensity of the white line is related to electronic structural changes around the absorbing atom, which depend on the nature of the ligands, coordination geometry and/or chemical environment. For both Tb and Gd XANES, the white line is

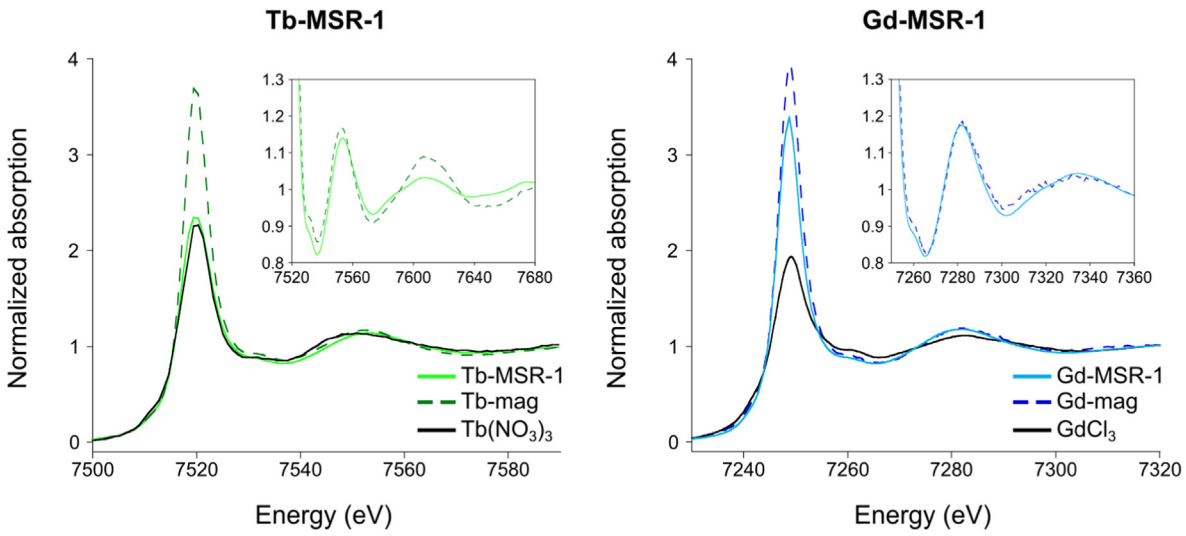

Fig. 1. Tb L_3-edge (left) and Gd L_3-edge (right) XANES spectra of Tb-MSR-1 and Gd-MSR-1 and corresponding isolated magnetosomes (Tb-mag and Gd-mag). Spectra of references for Tb^{3+} ($Tb(NO_3)_3$) and Gd^{3+} ($GdCl_3$) are displayed as well. Inset: detail of the post-edge oscillations.

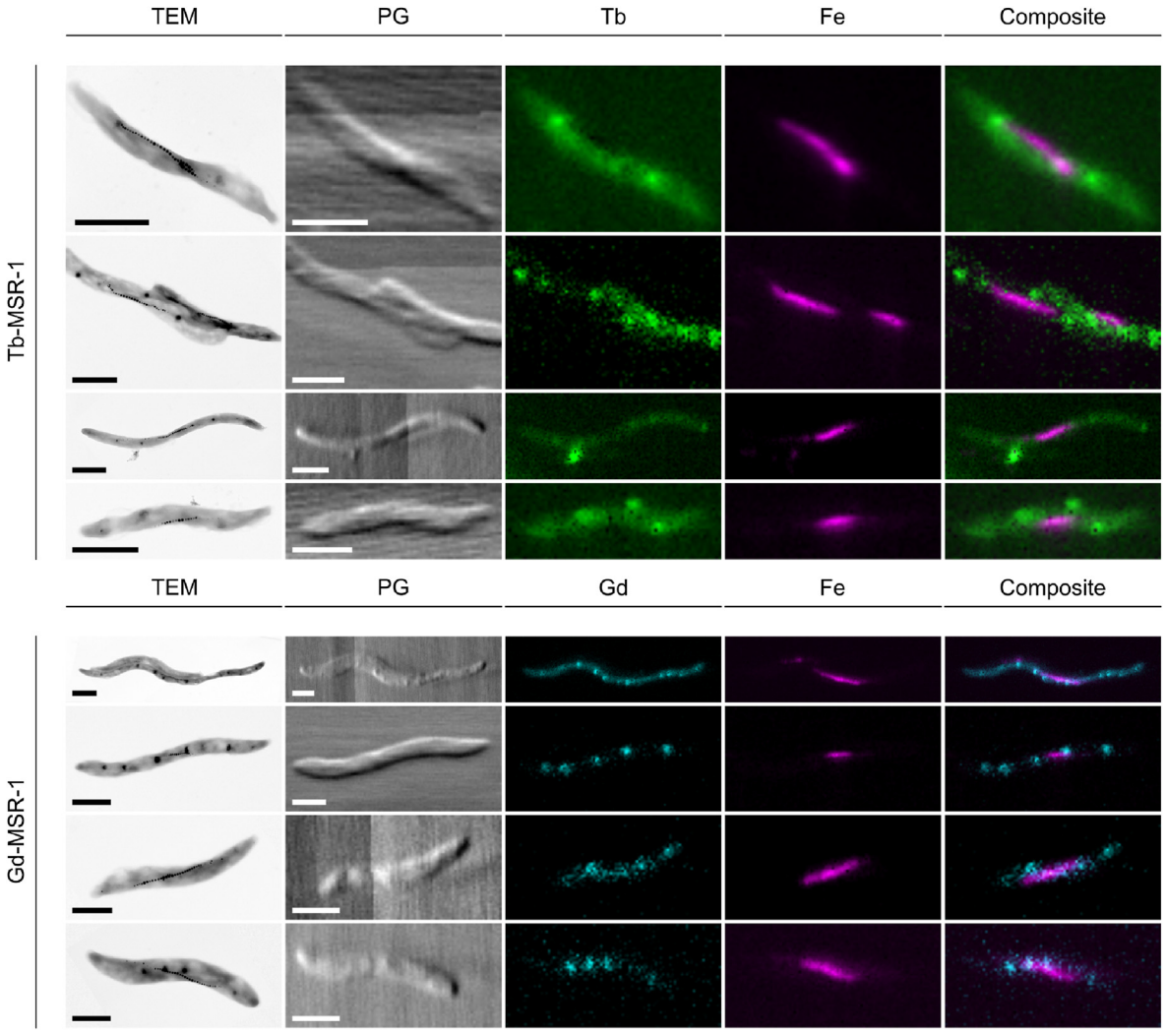

Fig. 2. TEM, phase-gradient (PG), and scanning X-ray fluorescence microscopy (SXFM) images of Tb-MSR-1 and Gd-MSR-1. For SXFM maps, the Tb/Gd $L\alpha_1$ XRF maps, Fe $K\alpha_1$ XRF maps, and the composite maps of individual bacteria are displayed.

more intense for the isolated magnetosomes than for the bacteria, while the post-edge oscillations also differ between them (see insets of Fig. 1). This suggests that the Tb^{3+} and Gd^{3+} ions incorporated by the bacteria are not only within the magnetosomes, but can also be found in additional cellular compartments where they are likely coordinated with biomolecules.

The presence of Tb and Gd in other bacterial compartments was confirmed by scanning X-ray fluorescence microscopy performed at the X-ray nanoprobe beamline (I-14) at Diamond Light Source (UK). This is a microscopy technique based on the characteristic fluorescence emission energies of elements that allows the localization of specific elements with sub-100 nm resolution. By discerning the different fluorescence peaks (Supplementary Information, Fig. S3), we could determine the spatial distribution of each element inside the bacteria. Moreover, the X-rays scattered by the bacteria were used to generate normalized phase-gradient (PG) images to observe the shape of the bacteria. As displayed in Fig. 2 the Fe is located forming a line in the middle of each bacterium that corresponds to the magnetosome chain on the TEM images. However, both Tb and Gd are distributed along the whole bacteria, forming clusters in some occasions. This confirms the data obtained by XANES that Tb and Gd are distributed throughout the bacteria and not only incorporated into the magnetosomes as we observed in our previous publication [27].

Finally, transmission electron microscopy (TEM) images of Tb-MSR-1 and Gd-MSR-1 (Fig. 3) show that the incorporation of Tb and Gd does not induce significant changes in the morphology of the bacteria and magnetosome chain arrangements with respect to the control MSR-1 grown in standard conditions. Details about the morphological characterization of the magnetosome chains can be found in Jefremovas *et al.* [27].

3.2. Theranostic potential of Tb-MSR-1 and Gd-MSR-1

In this section we will analyze the potential of Tb-MSR-1 and Gd-MSR-1 for theranostic applications. After confirming that the incorporation of Tb/Gd does not alter the heating efficiency of the modified bacteria for magnetic hyperthermia applications, we will analyze separately the additional diagnostic functionalities provided to MSR-1 *via* the incorporation of Tb (luminescence) and Gd (dual contrast for MRI). Finally, we will test the performance of Tb-MSR-1 and Gd-MSR-1 *in vitro* in two cell models.

3.2.1. Magnetic hyperthermia of Tb-MSR-1 and Gd-MSR-1

In magnetic hyperthermia, nanoparticles excited by alternating magnetic fields of amplitude H and frequency f generate heat that increases the temperature of the surrounding medium. The heating capacity is quantified through the specific absorption rate (SAR), which measures the capacity of the system to transform the absorbed magnetic energy into heat.

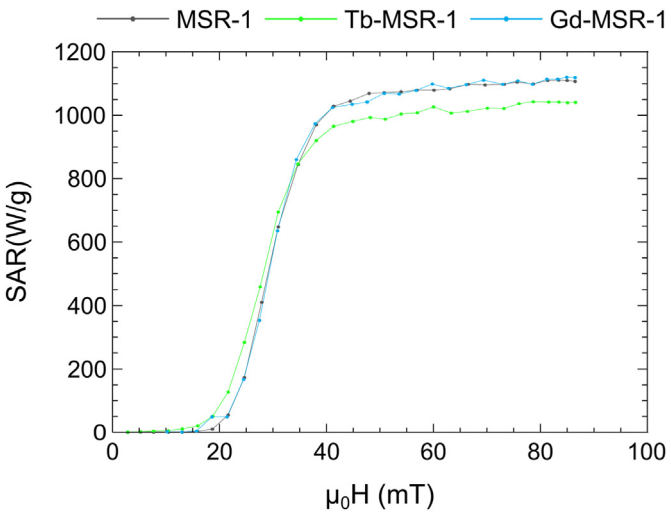

Fig. 4. Specific absorption rate (SAR) measured at $f = 133$ kHz corresponding to MSR-1, Tb-MSR-1, and Gd-MSR-1 dispersed in Milli-Q water.

Here, the SAR values of Tb-MSR-1 and Gd-MSR-1 dispersed in Milli-Q water were measured *via* an AC magnetometry method and compared to that of MSR-1 [10]. Measurements were carried out using an AC magnetic field of a fixed frequency $f = 133$ kHz and a magnetic field amplitude ($\mu_0 H$) of up to 90 mT in a custom-made equipment [37].

Fig. 4 shows the SAR values as a function of the magnetic field amplitude for Tb-MSR-1 and Gd-MSR-1 together with MSR-1. The SAR *vs.* H curves are similar for the three samples and follow the trend reported in other studies [10,39,40], so that for low applied magnetic fields the SAR value is negligible but increases significantly above 20 mT, reaching saturation at around 40 mT. There are no essential differences between the saturation values reached by MSR-1 and Gd-MSR-1 (1120 Wg^{-1} or 8.4 $Wg^{-1}kHz^{-1}$ if normalized by the frequency) and Tb-MSR-1, which is only 7% lower. These are among the highest values reported at clinically safe values of frequency and field amplitude [5], surpassing those typically obtained for iron oxide-based nanoparticles, which range between 2 and 5 $Wg^{-1}kHz^{-1}$ [40–43]. In sum, these results confirm that incorporating Tb/Gd into MSR-1 does not affect the outstanding heating efficiency of the MSR-1 bacteria.

3.2.2. Luminescence of Tb-MSR-1

Lanthanides such as Tb have been proposed as versatile molecular probes of biological systems due to their photophysical properties, including long luminescence lifetimes, narrow bandwidths, and insensitivity to chemical environment [44]. It is known that Tb^{3+} can replace

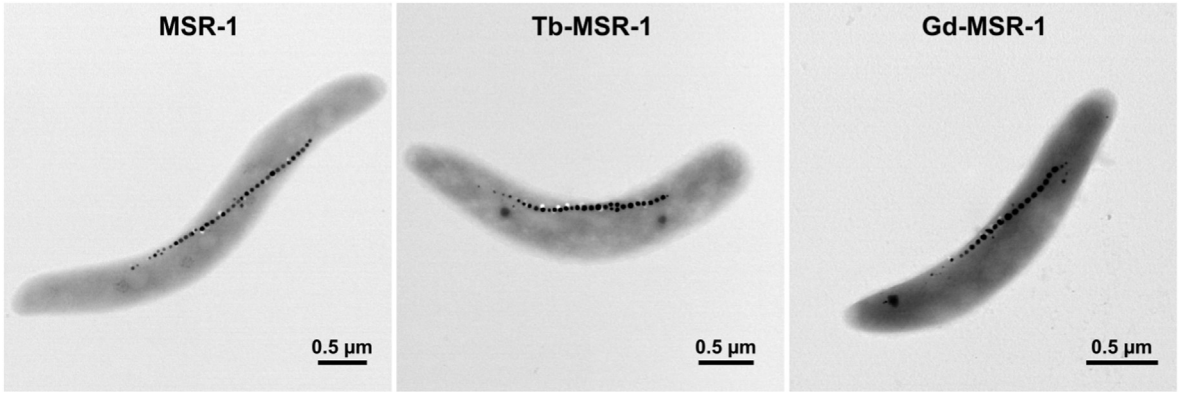

Fig. 3. Representative TEM images of MSR-1, Tb-MSR-1, and Gd-MSR-1.

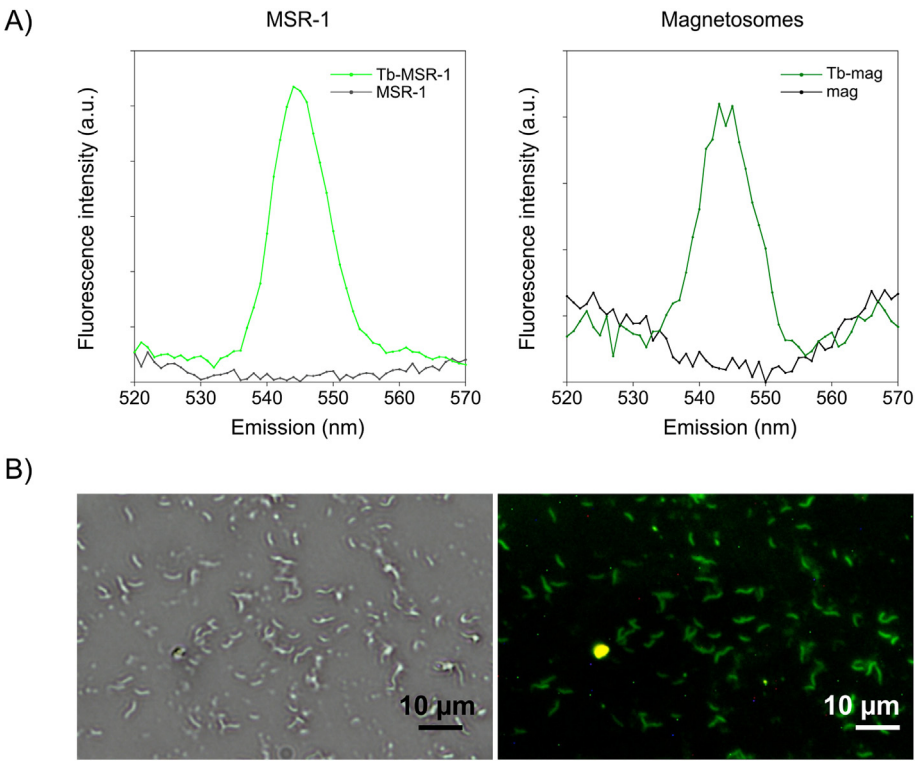

Fig. 5. A) Photoluminescence of Tb-MSR-1 and MSR-1 and their isolated magnetosomes (Tb-mag and mag) excited at $\lambda_{ex} = 285$ nm. B) Microscopy images of Tb-MSR-1. Bright field (left) and fluorescence (right) ($\lambda_{ex} = 350/50$ nm, $\lambda_{em} \geq 500$ nm).

Ca^{2+} in biological systems as they have a similar ionic radius (0.92 Å for Tb^{3+} and 0.99 Å for Ca^{2+}) [45]. As a result, Tb can form stable complexes with polypeptides replacing Ca^{2+}, and confers photoluminescence under UV excitation in the range of maximum protein absorption ($\lambda_{ex} = 285$ nm) showing a characteristic maximum emission peak at 545 nm [44,46]. Under this premise, the photoluminescence provided by the incorporation of Tb was tested with fluorimetry measurements and fluorescence microscopy.

The emission band was measured at 285 nm excitation in the range of 520–570 nm for four samples: *i)* Tb-MSR-1, *ii)* MSR-1, *iii)* magnetosomes isolated from Tb-MSR-1 (Tb-mag), and *iv)* magnetosomes isolated from MSR-1 (mag). As shown in Fig. 5A, both the Tb-MSR-1 and Tb-mag display the Tb-specific emission peak at 545 nm, whereas their corresponding control counterparts, MSR-1 and mag, do not show any fluorescence signal, confirming that the detected emission comes from Tb. In the case of the Tb-mag, the fluorescence emission occurring upon excitation with the maximum protein absorption wavelength suggests that Tb is linked to the proteins of the magnetosome membrane in addition to their presence in the mineral core, as inferred by XANES measurements.

The distribution of Tb in the bacteria is further evidenced by means of fluorescence microscopy imaging of Tb-MSR-1. Due to technical limitations, the sample could not be excited at the optimum wavelength of 285 nm. Alternatively, images were collected exciting Tb-MSR-1 with UV light using a band-pass filter (350/50 nm) and the emission was collected with a cut-off filter from 500 nm. Under these conditions, Fig. 5B shows bright field and fluorescence images of Tb-MSR-1.

Even though the spatial resolution and the measurement conditions were not optimal, the good agreement between bright field and fluorescence images of bacterial bodies demonstrates that the incorporation of Tb is a successful route towards the production of luminescent bacteria with applications, for example, as biomarker agents.

3.2.3. Gd-MSR-1 as dual contrast agents for magnetic resonance imaging

Magnetosomes are promising candidates as magnetic resonance imaging (MRI) contrast agents since magnetite nanoparticles provide negative contrast by shortening the T_2 transverse relaxation time [47–49]. On the other hand, paramagnetic substances, such as Gd- and Mn-based materials, act as positive contrast agents by shortening the T_1 longitudinal relaxation time.

MRI studies have been carried out in four samples, for comparison: *i)* Gd-MSR-1, *ii)* MSR-1, *iii)* magnetosomes isolated from Gd-MSR-1 (Gd-mag), and *iv)* magnetosomes isolated from MSR-1 (mag). In all cases, samples were suspended in water with Fe concentrations ranging from 0 mM to 0.36 mM and were measured in an 11.7 T MRI scanner.

Fig. 6A shows the T_1 and T_2 parametric maps obtained with increasing Fe content. These maps have been reconstructed from the T_1 images acquired with 12 increasing repetition time (TR) values (150–12500 ms) and from the T_2 images acquired with 32 increasing time-to-echo (TE) values (5–135 ms, delta = 5 ms) (see Figs. S4 and S5 in the Supplementary Information). The T_2 maps of all the samples reveal a clear shortening of the T_2 relaxation time when increasing the Fe content, indicating that they can work as T_2-shortening contrast agents, as expected for magnetite nanoparticles. Interestingly, while the T_1 maps of MSR-1, Gd-mag, and mag are essentially independent of the concentration of Fe, Gd-MSR-1 shows a contrast change with the Fe concentration, enabling a potential use of these bacteria as T_1-shortening contrast agents.

From T_1 and T_2 maps the contrast efficiency of the samples can be quantified. The contrast efficiency, or signal enhancement produced by a contrast agent, is measured by the longitudinal and transverse relaxivities, r_1 and r_2, respectively, which are obtained from the slope of the linear fits of the corresponding relaxation rates ($R_{i\ =\ 1,2} = 1/T_i$) *vs.* Fe concentration (Fig. 6B). The results of the relaxivities are shown in Table 1.

The r_2 values of all samples are similar, ranging between 315 and 370 $mM^{-1}s^{-1}$. This indicates that the incorporation of Gd^{3+} ions does not affect the T_2 contrast efficiency. Such an observation is reasonable considering the low Gd doping content of these magnetosome cores

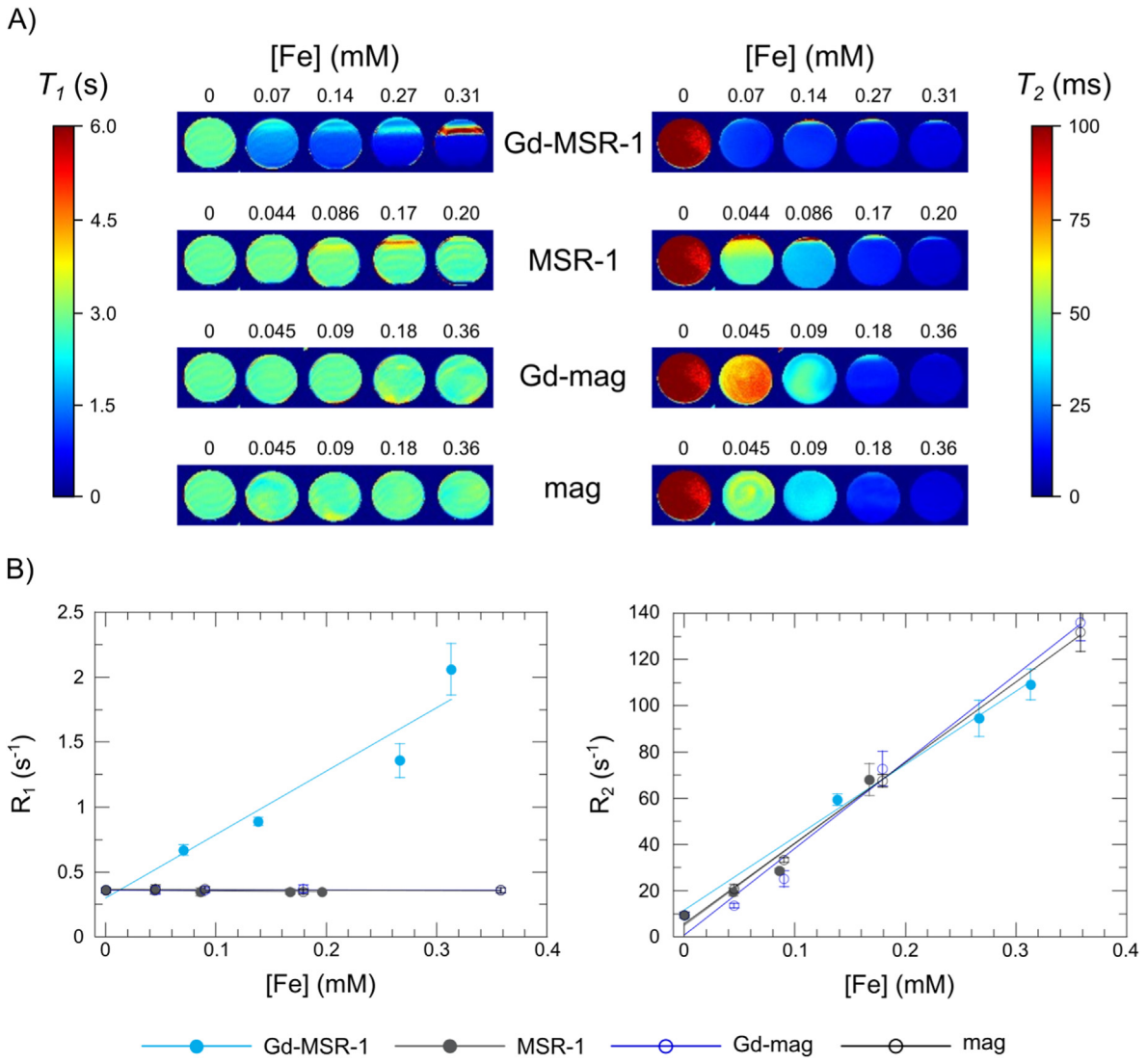

Fig. 6. A) T_1 (left) and T_2 (right) parametric maps obtained at increasing Fe concentrations at 11.7 T. B) Longitudinal ($R_1 = 1/T_1$) and transverse ($R_2 = 1/T_2$) relaxation rates *vs.* Fe concentration. The slopes of the linear fits give the relaxivities (r_1 and r_2) displayed in Table 1.

Table 1
Longitudinal (r_1) and transverse (r_2) relaxivities at 11.7 T obtained from the linear fittings in Fig. 6B.

	r_1 $(mM_{Fe})^{-1}$ s^{-1}	r_2 $(mM_{Fe})^{-1}$ s^{-1}
Gd-MSR-1	4.87	315.3
MSR-1	0.05	354.1
Gd-mag	0.00	375.9
mag	0.00	349.1

($\approx 3-4\%$, as estimated from XANES [27]), and the near absence of differences in the magnetic response of the MSR-1 and Gd-MSR-1 around room temperature [27]. The values obtained for r_2 are comparable to other values reported for magnetosomes in the literature (between 200 and 526 $mM^{-1}s^{-1}$ for fields ranging between 4.7 and 17.2 T) [47,50,51].

On the other hand, MSR-1, Gd-mag, and mag show negligible r_1 values, accordingly to the T_1 maps shown earlier, but Gd-MSR-1 stands out with a clear linear increase of the relaxation rate with the concentration, resulting in a r_1 value of 4.9 $mM^{-1}s^{-1}$. Thus, the incorporation of Gd adds T_1 contrasting capabilities to Gd-MSR-1.

In sum, these results showcase that Gd-MSR-1 are promising dual contrast agents for magnetic resonance imaging since, depending on the pulse sequence used for imaging, they will appear as positive in T_1 weighted images and as negative in T_2 weighted images. Dual contrast agents have recently gained increased attention for their use in clinical MRI [28,29]. A dual T_1/T_2 contrast agent produces a distinguishable contrast in both T_1-weighted and T_2-weighted images, facilitating their distinction from potential endogenous substances of the body that may provide contrast only in T_1 or T_2 modes [52].

3.2.4. In vitro assessment of the diagnostic potential of Tb-MSR-1 and Gd-MSR-1

The diagnostic functionalities acquired by MSR-1 through incorporation of Tb and Gd have been tested *in vitro* in two cell models: A549 lung carcinoma cells and RAW 264.7 macrophages.

First, we have analyzed the cytotoxicity of the bacteria. As reported previously [10], MSR-1 do not cause cytotoxicity in A549 lung carcinoma

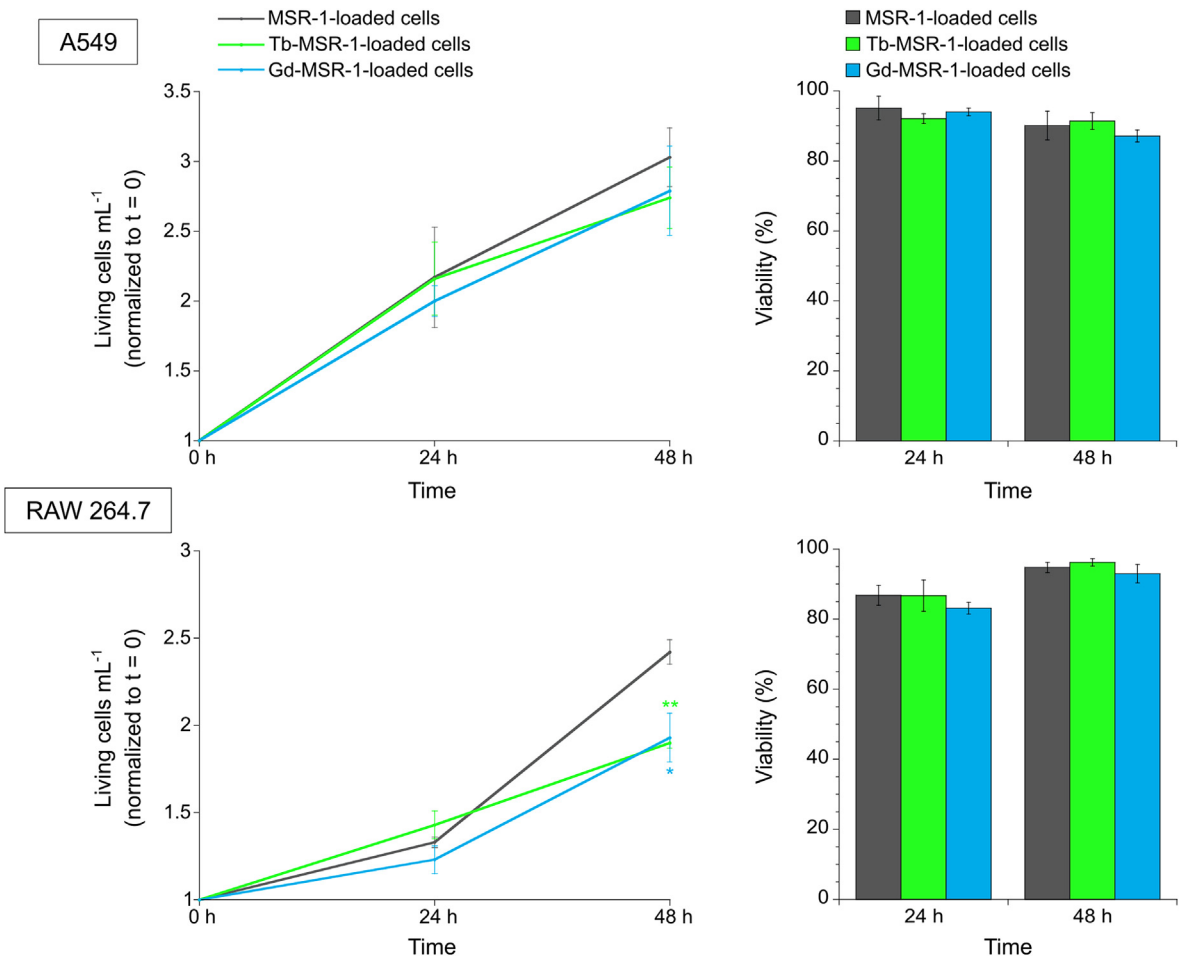

Fig. 7. Left: Time evolution of the number of living A549 and RAW 264.7 cells normalized to t = 0 h. Right: Viability percentages after 24 h and 48 h of culturing MSR-1/Tb-MSR-1/Gd-MSR-1-loaded A549 and RAW 264.7 cells. The results represent the mean ± standard deviation values, n = 3.

cells as they do not affect their viability nor their growing ability. Here we aim to verify whether Tb/Gd incorporation causes any change in MSR-1 cytotoxicity.

As observed in Fig. 7, cells continue to proliferate when incubated with MSR-1 (without or with Tb/Gd). However, it must be noted that in the case of RAW 264.7, there is a significant difference in cell proliferation after 48 h when the cells are incubated with Tb/Gd-MSR-1 in comparison to MSR-1.

To further investigate the cytotoxicity of the bacteria, we measured cell viability as the ratio between living and total number of cells. As observed in Fig. 7, there are no significant changes in cell viability after 24 h and 48 h of cell incubation with MSR-1, Tb-MSR-1, or Gd-MSR-1 as the mean value of viability in both cell types ranges between 87% and 96% after 48 h, indicating that the incorporation of Tb/Gd does not increase the cytotoxicity of MSR-1.

Then, aiming to test the diagnostic potential of Tb-MSR-1 and Gd-MSR-1 *in vitro*, both tested cell lines were incubated overnight with bacteria as explained in the Materials and Methods section.

Fig. 8A shows bright field and fluorescence images of control A549 cells and Tb-MSR-1-loaded A549 cells obtained in the same conditions as in Fig. 5B. As observed in the images, the control cells do not show any fluorescence when excited with UV light whereas cells incubated with Tb-MSR-1 do show fluorescence. Another conclusion that can be inferred from these images is that Tb-MSR-1 bacteria are inside the cells as they can be observed in the cytoplasm surrounding the nuclei that appear as non-fluorescent.

Regarding the contrasting performance of Gd-MSR-1, Fig. 8B shows the T_1 and T_2 parametric maps of control and Gd-MSR-1-loaded A549 and RAW 264.7 cells. These maps have been reconstructed from the T_1 and T_2 images presented in Figs. S6 and S7. While no contrast is observed in the control cells, the incorporation of Gd-MSR-1 produces a shortening of both T_1 and T_2 in both cell lines, proving the potential of Gd-MSR-1 as dual contrast agents.

4. Conclusions

The incorporation of Tb and Gd into *Magnetospirillum gryphiswaldense* MSR-1 improves their potential as biomedical agents because the bacteria retain the characteristics of the unmodified MSR-1 in terms of heating efficiency for magnetic hyperthermia and T_2 contrast for MRI, while adding supplementary functionalities. Tb-MSR-1 gain luminescence properties under UV excitation and Gd-MSR-1 turn into dual contrast agents for magnetic resonance imaging because Gd^{3+} adds T_1 contrast to the T_2 contrast provided by the magnetite cores of magnetosomes. Finally, we have verified that Tb-MSR-1 and Gd-MSR-1 are not cytotoxic and have demonstrated their new diagnostic functionalities *in vitro* in two cell models. Thus, we conclude that these lanthanide-modified MSR-1 could be potential biomedical agents with improved

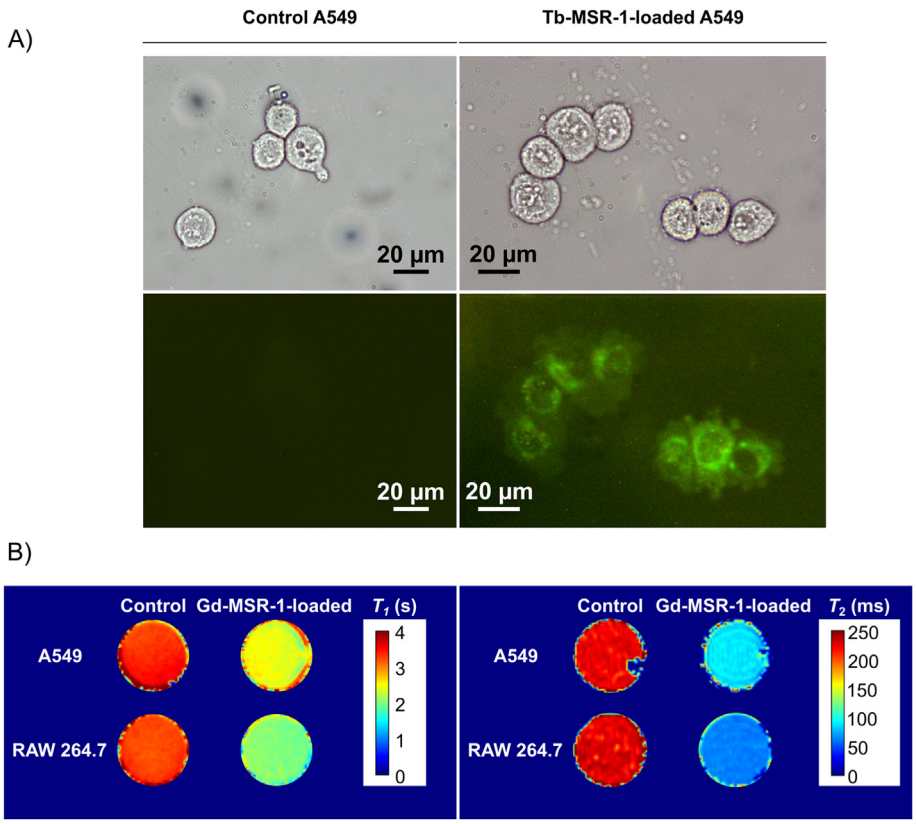

Fig. 8. A) Microscopy images of control and Tb-MSR-1-loaded A549 cells. Bright field (upper panel) and fluorescence (lower panel) (λ_{ex} = 350/50 nm, $\lambda_{em} \geq$ 500 nm). B) T_1 and T_2 parametric maps of control and Gd-MSR-1-loaded A549 and RAW 264.7 cells obtained at 11.7 T.

diagnostics capacities, further advancing magnetotactic bacteria as promising nanorobots.

Credit author statement

Lucía Gandarias: Data curation, Formal analysis, Investigation, Methodology, Writing – original draft, Writing – review & editing. **Elizabeth M. Jefremovas**: Investigation, Methodology, Writing – review & editing. **David Gandia**: Investigation, Writing – review & editing. **Lourdes Marcano**: Investigation, Writing – review & editing. **Virginia Martínez-Martínez**: Investigation, Writing – review & editing. **Pedro Ramos-Cabrer**: Investigation, Formal analysis, Writing – review & editing. **Daniel M. Chevrier**: Investigation, Formal analysis, Writing – review & editing. **Sergio Valencia**: Investigation, Writing – review & editing. **Luis Fernández Barquín**: Conceptualization, Project administration, Writing – review & editing. **M. Luisa Fdez-Gubieda**: Conceptualization, Methodology, Supervision, Project administration, Writing – review & editing. **Javier Alonso**: Conceptualization, Methodology, Project administration, Writing – review & editing. **Ana García-Prieto**: Investigation, Formal analysis, Project administration, Methodology, Supervision, Writing – original draft, Writing – review & editing. **Alicia Muela**: Conceptualization, Methodology, Supervision, Writing – original draft, Writing – review & editing.

Funding

This work has been funded by the Spanish Government (grants PID2020-115704RB-C31, PID2020-114347RB-C32, PID2020-115704RB-C33 and RED 2018–102626–T (HIPERNANO) funded by MCIN/AEI/10.13039/501100011033) and by the Basque Government (projects IT1479-22 and IT1639-22). LG acknowledges the Spanish Government for her PhD/Postdoctoral fellowship (PRE2018-083255 funded by MCIN/AEI/10.13039/501100011033 and by European Union Next GenerationEU/PRTR). EMJ acknowledges the Beca Concepción Arenal (Gobierno de Cantabria – Grant n. 406333) and Alexander von Humboldt Postdoctoral Fellowship. LM acknowledges the BBVA Foundation for the Leonardo Fellowships for Researchers and Cultural Creators 2022.

Declaration of competing interest

The authors declare that they have no known competing financial interests or personal relationships that could have appeared to influence the work reported in this paper.

Data availability

Data will be made available on request.

Acknowledgements

We acknowledge the BL22-CLÆSS beamline staff of the ALBA synchrotron for assistance during the experiment and the staff of the I-14 beamline at the Diamond Light Source, especially Dr. Miguel Gómez-González for his help during the experiment and the data analysis. We acknowledge the human and technical support provided by the microscopy services of SGIker (UPV/EHU). We thank Prof. José Ángel García, Dr. Iñaki Orue, and Danny Yosmar Villanueva-Álvaro for the hyperthermia measurements, and Sergio de la Vega for technical support.

Appendix A. Supplementary data

Supplementary data to this article can be found online at https://doi.org/10.1016/j.mtbio.2023.100680.

References

[1] D.A. Bazylinski, R.B. Frankel, Magnetosome formation in prokaryotes, Nat. Rev. Microbiol. 2 (3) (2004) 217–230.

[2] D. Faivre, D. Schüler, Magnetotactic bacteria and magnetosomes, Chem. Rev. 108 (11) (2008) 4875–4898.

[3] D.A. Bazylinski, C. Lefèvre, D. Schüler, Magnetotactic bacteria, in: E. Rosenberg, E.F. DeLong, S. Lory, E. Stackebrandt, F. Thompson (Eds.), The Prokaryotes, Springer, Berlin, Heidelberg, Berlin, Heidelberg, 2013, pp. 453–494.

[4] D.A. Bazylinski, C.T. Lefèvre, B.H. Lower, in: L.L. Barton, D.A. Bazylinski, H. Xu (Eds.), Magnetotactic Bacteria, Magnetosomes, and Nanotechnology, Nanomicrobiology, Springer, New York, NY, New York, NY, 2014, pp. 39–74.

[5] M.L. Fdez-Gubieda, J. Alonso, A. García-Prieto, A. García-Arribas, L. Fernández Barquín, A. Muela, Magnetotactic bacteria for cancer therapy, J. Appl. Phys. 128 (7) (2020), 070902.

[6] S.M. Kotakadi, D.P.R. Borelli, J.S. Nannepaga, Therapeutic applications of magnetotactic bacteria and magnetosomes: a review emphasizing on the cancer treatment, Front. Bioeng. Biotechnol. 10 (2022), 789016.

[7] E. Alphandéry, Applications of magnetotactic bacteria and magnetosome for cancer treatment: a review emphasizing on practical and mechanistic aspects, Drug Discov. Today 25 (8) (2020) 1444–1452.

[8] E. Alphandéry, S. Faure, O. Seksek, F. Guyot, I. Chebbi, Chains of magnetosomes extracted from AMB-1 magnetotactic bacteria for application in alternative magnetic field cancer therapy, ACS Nano 5 (8) (2011) 6279–6296.

[9] C. Chen, L. Chen, Y. Yi, C. Chen, L.F. Wu, T. Song, Killing of *Staphylococcus aureus* via magnetic hyperthermia mediated by magnetotactic bacteria, Appl. Environ. Microbiol. 82 (7) (2016) 2219–2226.

[10] D. Gandia, L. Gandarias, I. Rodrigo, J. Robles-García, R. Das, E. Garaio, J.Á. García, M. Phan, H. Srikanth, I. Orue, J. Alonso, A. Muela, M.L. Fdez-Gubieda, Unlocking the potential of magnetotactic bacteria as magnetic hyperthermia agents, Small 15 (41) (2019), 1902626.

[11] C. Chen, P. Wang, H. Chen, X. Wang, M.N. Halgamuge, C. Chen, T. Song, Smart magnetotactic bacteria enable the inhibition of neuroblastoma under an alternating magnetic field, ACS Appl. Mater. Interfaces 14 (12) (2022) 14049–14058.

[12] X. Chen, L. Lai, X. Li, X. Cheng, X. Shan, X. Liu, L. Chen, G. Chen, G. Huang, Magnetotactic bacteria AMB-1 with active deep tumor penetrability for magnetic hyperthermia of hypoxic tumors, Biomater. Sci. 10 (22) (2022) 6510–6516.

[13] O. Felfoul, M. Mohammadi, S. Taherkhani, D. de Lanauze, Y. Zhong Xu, D. Loghin, S. Essa, S. Jancik, D. Houle, M. Lafleur, L. Gaboury, M. Tabrizian, N. Kaou, M. Atkin, T. Vuong, G. Batist, N. Beauchemin, D. Radzioch, S. Martel, Magneto-aerotactic bacteria deliver drug-containing nanoliposomes to tumour hypoxic regions, Nat. Nanotechnol. 11 (11) (2016) 941–947.

[14] T. Gwisai, N. Mirkhani, M.G. Christiansen, T.T. Nguyen, V. Ling, S. Schuerle, Magnetic torque-driven living microrobots for increased tumor infiltration, Science Robotics 7 (71) (2022), eabo0665.

[15] R. Chaturvedi, Y. Kang, Y. Eom, S.R. Torati, C. Kim, Functionalization of biotinylated polyethylene glycol on live magnetotactic bacteria carriers for improved stealth properties, Biology 10 (10) (2021) 993.

[16] S. Martel, M. Mohammadi, O. Felfoul, Z. Lu, P. Pouponneau, Flagellated magnetotactic bacteria as controlled MRI-trackable propulsion and steering systems for medical nanorobots operating in the human microvasculature, Int. J. Robot Res. 28 (4) (2009) 571–582.

[17] M.R. Benoit, D. Mayer, Y. Barak, I.Y. Chen, W. Hu, Z. Cheng, S.X. Wang, D.M. Spielman, S.S. Gambhir, A. Matin, Visualizing implanted tumors in mice with magnetic resonance imaging using magnetotactic bacteria, Clin. Cancer Res. 15 (16) (2009) 5170–5177.

[18] M. Mahmoudi, A. Tachibana, A.B. Goldstone, Y.J. Woo, P. Chakraborty, K.R. Lee, C.S. Foote, S. Piecewicz, J.C. Barrozo, A. Wakeel, B.W. Rice, C.B. Bell, P.C. Yang, Novel MRI contrast agent from magnetotactic bacteria enables *in vivo* tracking of iPSC-derived cardiomyocytes, Sci. Rep. 6 (2016), 26960.

[19] A.V. Makela, M.A. Schott, C.S. Madsen, E.M. Greeson, C.H. Contag, Magnetic particle imaging of magnetotactic bacteria as living contrast agents is improved by altering magnetosome arrangement, Nano Lett. 22 (12) (2022) 4630–4639.

[20] S. Staniland, W. Williams, N. Telling, G. Van Der Laan, A. Harrison, B. Ward, Controlled cobalt doping of magnetosomes *in vivo*, Nat. Nanotechnol. 3 (2008) 158–162.

[21] D. Muñoz, L. Marcano, R. Martín-Rodríguez, L. Simonelli, A. Serrano, A. García-Prieto, M.L. Fdez-Gubieda, A. Muela, Magnetosomes could be protective shields against metal stress in magnetotactic bacteria, Sci. Rep. 10 (2020), 11430.

[22] L. Marcano, I. Orue, A. García-Prieto, R. Abrudan, J. Alonso, L. Fernández Barquín, S. Valencia, A. Muela, M.L. Fdez-Gubieda, Controlled magnetic anisotropy in single domain Mn-doped biosynthesized nanoparticles, J. Phys. Chem. C 124 (41) (2020) 22827–22838.

[23] L. Marcano, D. Muñoz, R. Martín-Rodríguez, I. Orue, J. Alonso, A. García-Prieto, A. Serrano, S. Valencia, R. Abrudan, L. Fernández Barquín, A. García-Arribas, A. Muela, M.L. Fdez-Gubieda, Magnetic study of Co-doped magnetosome chains, J. Phys. Chem. C 122 (13) (2018) 7541–7550.

[24] J. Li, N. Menguy, M.-A. Arrio, P. Sainctavit, A. Juhin, Y. Wang, H. Chen, O. Bunau, E. Otero, P. Ohresser, Y. Pan, Controlled cobalt doping in the spinel structure of magnetosome magnetite: new evidences from element- and site-specific X-ray magnetic circular dichroism analyses, J. R. Soc. Interface 13 (121) (2016), 20160355.

[25] T. Prozorov, T. Perez-Gonzalez, C. Valverde-Tercedor, C. Jimenez-Lopez, A. Yebra-Rodriguez, A. Körnig, D. Faivre, S.K. Mallapragada, P.A. Howse, D.A. Bazylinski, R. Prozorov, Manganese incorporation into the magnetosome magnetite: magnetic signature of doping, Eur. J. Mineral 26 (4) (2014) 457–471.

[26] M. Tanaka, R. Brown, N. Hondow, A. Arakaki, T. Matsunaga, S. Staniland, Highest levels of Cu, Mn and Co doped into nanomagnetic magnetosomes through optimized biomineralisation, J. Mater. Chem. 22 (2012), 11919.

[27] E.M. Jefremovas, L. Gandarias, L. Marcano, A. García-Prieto, I. Orue, A. Muela, M.L. Fdez-Gubieda, L. Fernández Barquín, J. Alonso, Modifying the magnetic response of magnetotactic bacteria: incorporation of Gd and Tb ions into the magnetosome structure, Nanoscale Adv. 4 (12) (2022) 2649–2659.

[28] G.H. Im, S.M. Kim, D.-G. Lee, W.J. Lee, J.H. Lee, I.S. Lee, Fe_3O_4/MnO hybrid nanocrystals as a dual contrast agent for both T_1- and T_2-weighted liver MRI, Biomaterials 34 (8) (2013) 2069–2076.

[29] F. Li, D. Zhi, Y. Luo, J. Zhang, X. Nan, Y. Zhang, W. Zhou, B. Qiu, L. Wen, G. Liang, Core/shell Fe_3O_4/Gd_2O_3 nanocubes as T_1-T_2 dual modal MRI contrast agents, Nanoscale 8 (25) (2016) 12826–12833.

[30] U. Heyen, D. Schüler, Growth and magnetosome formation by microaerophilic *Magnetospirillum* strains in an oxygen-controlled fermentor, Appl. Microbiol. Biotechnol. 61 (5–6) (2003) 536–544.

[31] K. Grünberg, C. Wawer, B.M. Tebo, D. Schüler, A large gene cluster encoding several magnetosome proteins is conserved in different species of magnetotactic bacteria, Appl. Environ. Microbiol. 67 (10) (2001) 4573–4582.

[32] B. Ravel, M. Newville, ATHENA, artemis, HEPHAESTUS: data analysis for X-ray absorption spectroscopy using IFEFFIT, J. Synchrotron Radiat. 12 (Pt 4) (2005) 537–541.

[33] M. Newville, IFEFFIT: interactive XAFS analysis and FEFF fitting, J. Synchrotron Radiat. 8 (Pt 2) (2001) 322–324.

[34] P.D. Quinn, L. Alianelli, M. Gomez-Gonzalez, D. Mahoney, F. Cacho-Nerin, A. Peach, J.E. Parker, The hard X-ray nanoprobe beamline at Diamond light source, J. Synchrotron Radiat. 28 (2021) 1006–1013.

[35] P.D. Quinn, F. Cacho-Nerin, M.A. Gomez-Gonzalez, J.E. Parker, T. Poon, J.M. Walker, Differential phase contrast for quantitative imaging and spectro-microscopy at a nanoprobe beamline, J. Synchrotron Radiat. 30 (1) (2023) 200–207.

[36] V.A. Solé, E. Papillon, M. Cotte, P. Walter, J. Susini, A multiplatform code for the analysis of energy-dispersive X-ray fluorescence spectra, Spectrochim. Acta B Atom Spectrosc. 62 (1) (2007) 63–68.

[37] I. Rodrigo, I. Castellanos-Rubio, E. Garaio, O.K. Arriortua, M. Insausti, I. Orue, J.Á. García, F. Plazaola, Exploring the potential of the dynamic hysteresis loops via high field, high frequency and temperature adjustable AC magnetometer for magnetic hyperthermia characterization, Int. J. Hyperther. 37 (1) (2020) 976–991.

[38] I. Andreu, E. Natividad, Accuracy of available methods for quantifying the heat power generation of nanoparticles for magnetic hyperthermia, Int. J. Hyperther. 29 (8) (2013) 739–751.

[39] A. Muela, D. Muñoz, R. Martín-Rodríguez, I. Orue, E. Garaio, A. Abad Díaz de Cerio, J. Alonso, J.Á. García, M.L. Fdez-Gubieda, Optimal parameters for hyperthermia treatment using biomineralized magnetite nanoparticles: theoretical and experimental approach, J. Phys. Chem. C 120 (42) (2016) 24437–24448.

[40] Z. Nemati, J. Alonso, I. Rodrigo, R. Das, E. Garaio, J.Á. García, I. Orue, M.-H. Phan, H. Srikanth, Improving the heating efficiency of iron oxide nanoparticles by tuning their shape and size, J. Phys. Chem. C 122 (4) (2018) 2367–2381.

[41] P. Guardia, R. Di Corato, L. Lartigue, C. Wilhelm, A. Espinosa, M. Garcia-Hernandez, F. Gazeau, L. Manna, T. Pellegrino, Water-soluble iron oxide nanocubes with high values of specific absorption rate for cancer cell hyperthermia treatment, ACS Nano 6 (4) (2012) 3080–3091.

[42] I. Castellanos-Rubio, O. Arriortua, D. Iglesias-Rojas, A. Barón, I. Rodrigo, L. Marcano, J.S. Garitaonandia, I. Orue, M.L. Fdez-Gubieda, M. Insausti, A milestone in the chemical synthesis of Fe_3O_4 nanoparticles: unreported bulklike properties lead to a remarkable magnetic hyperthermia, Chem. Mater. 33 (22) (2021) 8693–8704.

[43] E.M. Jefremovas, L. Gandarias, I. Rodrigo, L. Marcano, C. Grüttner, J.Á. García, E. Garayo, I. Orue, A. García-Prieto, A. Muela, M.L. Fernández-Gubieda, J. Alonso, L.F. Barquín, Nanoflowers versus magnetosomes: comparison between two promising candidates for magnetic hyperthermia therapy, IEEE Access 9 (2021) 99552–99561.

[44] U. Cho, J.K. Chen, Lanthanide-based optical probes of biological systems, Cell Chem. Biol. 27 (8) (2020) 921–936.

[45] H.G. Brittain, F.S. Richardson, R.B. Martin, Terbium(III) emission as a probe of calcium(II) binding sites in proteins, J. Am. Chem. Soc. 98 (25) (1976) 8255–8260.

[46] M.H. Simonian, J.A. Smith, Spectrophotometric and colorimetric determination of protein concentration, Curr. Protoc. Mol. Biol. 76 (2006), 1902626.

[47] S. Mériaux, M. Boucher, B. Marty, Y. Lalatonne, S. Prévéral, L. Motte, C.T. Lefèvre, F. Geffroy, F. Lethimonnier, M. Péan, D. Garcia, G. Adryanczyk-Perrier, D. Pignol, N. Ginet, Magnetosomes, biogenic magnetic nanomaterials for brain molecular imaging with 17.2 T MRI scanner, Adv. Healthc. Materi. 4 (7) (2015) 1076–1083.

[48] Z. Xiang, X. Yang, J. Xu, W. Lai, Z. Wang, Z. Hu, J. Tian, L. Geng, Q. Fang, Tumor detection using magnetosome nanoparticles functionalized with a newly screened EGFR/HER2 targeting peptide, Biomaterials 115 (2017) 53–64.

[49] M. Boucher, F. Geffroy, S. Prévéral, L. Bellanger, E. Selingue, G. Adryanczyk-Perrier, M. Péan, C.T. Lefèvre, D. Pignol, N. Ginet, S. Mériaux, Genetically tailored

magnetosomes used as MRI probe for molecular imaging of brain tumor, Biomaterials 121 (2017) 167–178.
[50] G. Jiang, D. Fan, J. Tian, Z. Xiang, Q. Fang, Self-confirming magnetosomes for tumor-targeted T_1/T_2 dual-mode mri and mri-guided photothermal therapy, Adv. Healthc. Materi. 11 (14) (2022), 2200841.
[51] T. Orlando, S. Mannucci, E. Fantechi, G. Conti, S. Tambalo, A. Busato, C. Innocenti, L. Ghin, R. Bassi, P. Arosio, F. Orsini, C. Sangregorio, M. Corti, M.F. Casula, P. Marzola, A. Lascialfari, A. Sbarbati, Characterization of magnetic nanoparticles from *Magnetospirillum gryphiswaldense* as potential theranostics tools, Contrast Media Mol. Imaging 11 (2) (2016) 139–145.
[52] Z. Zhou, R. Bai, J. Munasinghe, Z. Shen, L. Nie, X. Chen, T_1–T_2 dual-modal magnetic resonance imaging: from molecular basis to contrast agents, ACS Nano 11 (6) (2017) 5227–5232.